THE ASTROPHYSICAL JOURNAL, 477:235–240, 1997 March 1

ASTROPHYSICAL EXTENDED X-RAY ABSORPTION FINE-STRUCTURE ANALYSIS

JONATHAN W. WOO AND ROBERT C. FORREY
Harvard-Smithsonian Center for Astrophysics, 60 Garden Street, Cambridge, MA 02138
AND
KYEONGJAE CHO[1]
Department of Physics, Massachusetts Institute of Technology, Cambridge, MA 02139
Received 1996 August 7; accepted 1996 September 23

ABSTRACT

We present an astrophysical extended X-ray absorption fine-structure (EXAFS) analysis (AEA) tool. The AEA tool is designed to generate a numerical model of the modification to the X-ray absorption coefficient due to the EXAFS phenomenon. We have constructed a complete database (elements up to the atomic number 92) of EXAFS parameters: central atom phase shift ($2\delta_1$), backscattering phase shift (ϕ_b), and backscattering amplitude (F). Using the EXAFS parameter data base, the AEA tool can generate a numerical model of any compound when the atomic numbers of neighboring atoms and their distances to the central X-ray–absorbing atom are given.

Subject headings: atomic processes — ISM: abundances — X-rays: general

1. INTRODUCTION

The current development of high-resolution ($E/\Delta E \sim 1000$) X-ray spectrometers on board future satellite missions (e.g., *Advanced X-ray Astrophysics Facility*, i.e., *AXAF*) has opened a new window to study the properties of interstellar grains and molecules by analyzing the X-ray absorption fine structure (XAFS) in the observed spectra of X-rays that have passed through interstellar matter (Woo 1995). XAFS is produced by the interference effect of the backscattered photoelectron wave from nearby atoms on the final state of the outgoing photoelectron wave. Therefore, XAFS is dependent on the type, structure, and state of the intervening matter. Since XAFS reflects deeper probing of interstellar medium (ISM) than any other traditional method of ISM study (e.g., optical, UV), we should be able to use XAFS to explore previously unknown properties of the interstellar molecules and grains (Martin 1970; Evans 1986). In efforts to develop high-resolution X-ray spectrometers, the instrument calibrations frequently have to deal with XAFS in their own instrumental response (see, e.g., Owens et al. 1997). Therefore, it is useful to provide the astrophysical community with suitable theoretical tools and an easily accessible database to model XAFS.

XAFS is typically divided into two regions with respect to the photoelectron momentum k: the low-energy region ($k < 4$ Å^{-1}), which produces the X-ray absorption near edge structure (XANES), and the high-energy region ($k > 4$ Å^{-1}), which produces the extended X-ray absorption fine structure (EXAFS). The high-energy region is dominated by single scattering of the photoelectrons from immediate neighboring atoms, whereas the low-energy region is dominated by multiple scattering. Although the theoretical formulation of XAFS was done early on (XANES by Kossel 1920; EXAFS by Kronig 1931), the practical usage of XAFS to probe the structure of molecular and solid-state matter was recognized much later by Sayers, Stern, & Lytle (1971) when modern synchrotron light-source technology became available.

As the first of our series on XAFS analysis, we will present the astrophysical EXAFS analysis (AEA) tool. Subsequent papers in this series will present the astrophysical XANES analysis (AXA) tool (see, e.g., Cho & Woo 1997). We have designed these tools so that a user with a limited understanding of the theoretical aspects of numerical modeling can easily access the databases and use them to study XAFS within a limited personal/workstation computer facility. Our theoretical model of the current AEA tool is generally based on Lee & Beni (1977) and Teo & Lee (1979). A brief overview of our theoretical model is made in § 2. In § 3, we describe the AEA tool that constructs an EXAFS model for any given compound.

2. THEORETICAL EXAFS MODEL

The EXAFS phenomenon can be modeled as the modification to the X-ray absorption coefficient of an isolated atom due to the coherent interference effect of the scattering photoelectron wave from the neighboring atom and the original outgoing photoelectron wave generated from the central X-ray–absorbing atom. The initial state consists of a many-atom system (molecule or condensed matter) and an X-ray with its energy substantially above the ionization energy of the X-ray–absorbing atom ($k > 4$ Å^{-1}), and the final state consists of the many-atom system and the ejected photoelectron. The detailed formulation of the single-particle EXAFS theory can be found in many articles (see, e.g., Lee & Pendry 1975); therefore, we give only a brief outline of the theory here.

The oscillatory absorption coefficient of EXAFS normalized to a smooth absorption coefficient μ_0 of an isolated atom is given by

$$\chi = \frac{\mu - \mu_0}{\mu_0}, \tag{1}$$

where μ is the absorption coefficient of the center atom of the many-atom system (molecule or condensed matter). The X-ray absorption coefficient μ can be calculated by Fermi's Golden Rule within the dipole approximation for the photon-induced transition of an electron from initial state

[1] Also Department of Physics and Division of Applied Sciences, Harvard University.

$|i\rangle$ to a final state $|f\rangle$

$$\mu \sim |\langle f|\hat{\epsilon}\cdot \boldsymbol{r}|i\rangle|^2 , \quad (2)$$

where $\hat{\epsilon}$ is the polarization vector of the photon and $\boldsymbol{r}$ is the electron coordinate. For a K-edge transition, $|i\rangle$ is the 1s core state of the X-ray–absorbing atom. For an isolated atom, the final state $|f_0\rangle$ consists of the ionized atom plus the ejected photoelectron. The full final state $|f\rangle$ is defined to be

$$|f\rangle = \left(1 + \sum_j M_j\right)|f_0\rangle , \quad (3)$$

where M_j gives the modification of the final state due to backscattering from the jth neighboring atom. Substituting equation (3) into equation (2) we get

$$\mu \sim \mu_0\left(1 + \sum_j M_j + \text{complex conjugate}\right), \quad (4)$$

where the backscattered wave is assumed to be weak enough that the squared term can be neglected. The oscillatory absorption coefficient is obtained from equations (1) and (4) to be

$$\chi(k) = 2\sum_j \text{Re}\,(M_j) . \quad (5)$$

Following Lee & Pendry (1975), M_j is given by

$$M_j = \frac{\sum_{m_0}\sum_{lm}\sum_{l'm'} P_{l_0m_0,lm} Z^j_{lm,l'm'} P_{l'm',l_0m_0} e^{i(\delta_l+\delta_{l'})}}{\sum_{m_0}\sum_{lm}|P_{l_0m_0,lm}|^2} , \quad (6)$$

where $P_{l_0m_0,lm} = \langle l_0 m_0|e\hat{\epsilon}\cdot \boldsymbol{r}|lm\rangle$ is the dipole transition matrix from the initial state $|l_0 m_0\rangle$ to an excited state $|lm\rangle$, and $Z^j_{lm,l'm'}$ is the transition matrix that connects the outgoing photoelectron wave function $|l'm'\rangle$ from the central atom to the wave function $|lm\rangle$ that has been produced from the backscattering of the original outgoing wave by the neighboring atom j. δ_l and $\delta_{l'}$ are the respective phase shifts of the outgoing wave function $|l'm'\rangle$ and the backscattering wave function $|lm\rangle$. For an s core level ($l_0 = 0$), both l and l' should be 1, so that

$$M_j = \frac{\sum_m\sum_{m'} P_{00,1m} Z^j_{1m,1m'} P_{1m',00} e^{2i\delta_1}}{\sum_m |P_{00,1m}|^2} . \quad (7)$$

For unpolarized X-rays, it further reduces to

$$M_j = \tfrac{1}{3}\sum_m Z^{(j)}_{1m,1m} e^{2i\delta_1} . \quad (8)$$

A brief derivation of the general Z matrix is as follows. $Z_{lm,l'm'}$ relates the backscattered photoelectron wave function $\Psi^{(-)}_{\boldsymbol{k}}$ to the initial outgoing spherical photoelectron waves $j_l(kr)Y_{lm}(\hat{r})$ as

$$\Psi^{(-)}_{\boldsymbol{k}}(\boldsymbol{r}) = 2\sum_{lm} Z^{(j)}_{lm,l'm'} j_l(kr) Y_{lm}(\hat{r}) . \quad (9)$$

The desired matrix element $Z^{(j)}_{lm,l'm'}$ is derived by assuming that the outgoing and incoming photoelectron wave functions can be approximated by the plane waves

$$\Psi^{(+)}_{\boldsymbol{k}}(\boldsymbol{r}) = \Phi_{\text{out}}(\boldsymbol{r}_j)\exp\,[i\boldsymbol{k}\cdot(\boldsymbol{r}-\boldsymbol{r}_j)] \quad (10)$$

$$\Psi^{(-)}_{\boldsymbol{k}}(\boldsymbol{r}) = \Phi_{\text{in}}(\boldsymbol{r}=0)\exp\,(-i\boldsymbol{k}\cdot\boldsymbol{r}) , \quad (11)$$

where $\boldsymbol{r}_j$ is the position of the jth neighboring atom from the center atom and $\boldsymbol{k} = k\hat{r}_j$. The amplitudes of the plane waves are given by

$$\Phi_{\text{out}}(\boldsymbol{r}_j) = Y_{lm}(\hat{r}_j)h^{(+)}_l(kr_j) \quad (12)$$

$$\Phi_{\text{in}}(\boldsymbol{r}) = \Phi_{\text{out}}(\boldsymbol{r}_j)\sum_{lm} A_l\, Y^*_{lm}(\hat{r}_j)Y_{lm}(\hat{\boldsymbol{R}}_j)h^{(+)}_l(kR_j) , \quad (13)$$

where $h^{(+)}_l$ is the outgoing Hankel function and $\boldsymbol{R}_j = \boldsymbol{r} - \boldsymbol{r}_j$. Equation (13) relates the amplitude of the returning photoelectron wave to the amplitude of the original outgoing wave modified by scattering from the jth atom. The modification is given by the amplitude $A_l = 2\pi i^l(S_l - 1)$, where S_l is the scattering matrix element (see below). Using the addition theorem for spherical harmonics, we have

$$\Phi_{\text{in}}(\boldsymbol{r}=0) = \Phi_{\text{out}}(\boldsymbol{r}_j)\sum_l\left(\frac{2l+1}{4\pi}\right)A_l\,P_l(\cos\pi)h^{(+)}_l(kr_j) . \quad (14)$$

When $kr_j \gg 1$, the asymptotic expansion $h^+_l(kr_j) \sim (-i)^{l+1}\exp\,(ikr_j)/kr_j$ can be used in equation (14), leading to the result

$$\Phi_{\text{in}}(\boldsymbol{r}=0) = \frac{1}{r_j}\exp\,(ikr_j)f_k(\pi)\Phi_{\text{out}}(\boldsymbol{r}_j)$$

$$= \frac{1}{kr_j^2}(-i)^{l+1}\exp\,(2ikr_j)f_k(\pi)Y_{lm}(\hat{r}_j) , \quad (15)$$

where

$$f_k(\theta) = \frac{1}{2ik}\sum_{l=0}^{\infty}(2l+1)(S_l - 1)P_l(\cos\theta) \quad (16)$$

is the well-known scattering amplitude. Substituting equation (15) into equation (11), expanding the plane wave, and matching to equation (9) gives

$$Z^{(j)}_{lm,l'm'} = 2\pi i^{l'}Y^*_{l'm'}(-\hat{r}_j)\Phi_{\text{in}}(\boldsymbol{r}=0) \quad (17)$$

$$\sum_m Z^{(j)}_{lm,lm} = \frac{(-1)^l}{2ikr_j^2}(2l+1)f_k(\pi)\exp\,(2ikr_j) . \quad (18)$$

For an s wave initial state, $l = 1$ and

$$M_j = -f_k(\pi)\frac{\exp\,(2ikr_j + 2i\delta_1)}{2ikr_j^2} . \quad (19)$$

Using equations (5) and (19) along with the definitions $F(k) = |f_k(\pi)|$, $\phi_b(k) = \arg\,[f_k(\pi)]$, and $\eta(k) = 2\delta_1 + \phi_b(k) - \pi$ gives the result

$$\chi(k) = \sum_j F_j(k)\frac{\sin\,[2kr_j + \eta_j(k)]}{kr_j^2} . \quad (20)$$

The above derivation shows that the EXAFS calculation (eq. [20]) is simply reduced to obtaining a complete set of $2\delta_1$, ϕ_b, and F for all relevant atoms as a function of k. This information can typically be obtained by solving two potential scattering problems (ϕ_b and F from the neighboring atom; $2\delta_1$ from the central atom). Therefore, we provide an overview of potential scattering theory in the next subsection. The potential of the many-atom system is treated using the muffin tin approximation, where within a sphere centered about each atom the core potential is spherically symmetric and outside the spheres the potential is averaged and set to a constant value. The details of the potential energy function are provided in § 2.2.

2.1. *Scattering Calculation*

This section provides an overview of the scattering theory used in the present work. For a more detailed treatment, see standard textbooks such as Joachain (1975). The partial

wave Schrödinger equation for a central potential $V(r)$ is given by

$$-\frac{\hbar^2}{2\mu}\left[\frac{d^2}{dr^2}+k^2-\frac{l(l+1)}{r^2}\right]\psi_l(r)+V(r)\psi_l(r)=0\ , \quad (21)$$

where k is the relative momentum of the colliding particles and μ is their reduced mass. At large distances r, the potential tends to zero, and the differential equation (21) has the two solutions

$$u_{\pm}(r)=\exp\left[\pm i(kr-l\pi/2)\right]\ . \quad (22)$$

The wave function ψ_l behaves asymptotically as a superposition of the two solutions (eq. [22]) with the outgoing wave u_+ weighted by the scattering coefficient

$$S_l=\exp\left(2i\delta_l\right)\ . \quad (23)$$

The phase shift δ_l depends on the details of the potential $V(r)$ and is real for purely elastic collisions. For inelastic processes, the phase shift becomes complex owing to the removal of particles from the incident channel. The absorption factor

$$A_l=\exp\left(-2\ \mathrm{Im}\ \delta_l\right) \quad (24)$$

is assumed to contain the effects of all inelastic processes. The absorption factor A_l and the elastic phase shift Re δ_l can be calculated from a complex "optical" potential

$$V(r)=V_1(r)+iV_2(r)\ . \quad (25)$$

The definition

$$\psi_l(r)=u_1(r)+iu_2(r) \quad (26)$$

and the optical potential (eq. [25]) are used in equation (21), where the functions u_1 and u_2 are to be determined by the matrix equation

$$\begin{pmatrix} T-E+V_1 & -V_2 \\ V_2 & T-E+V_1 \end{pmatrix}\begin{pmatrix} u_1 \\ u_2 \end{pmatrix}=\begin{pmatrix} 0 \\ 0 \end{pmatrix} \quad (27)$$

with

$$T=-\frac{\hbar^2}{2\mu}\left[\frac{d^2}{dr^2}-\frac{l(l+1)}{r^2}\right]. \quad (28)$$

The eigenvector matrix is computed numerically and matched to the large-r asymptotic boundary condition

$$\begin{pmatrix} u_{11} & u_{12} \\ u_{21} & u_{22} \end{pmatrix}\sim-\begin{pmatrix} u_- & 0 \\ 0 & u_- \end{pmatrix}+\begin{pmatrix} S_{11} & S_{12} \\ S_{21} & S_{22} \end{pmatrix}\begin{pmatrix} u_+ & 0 \\ 0 & u_- \end{pmatrix}. \quad (29)$$

The result

$$u_{11}(r)+iu_{21}(r)\sim-u_-(r)+(S_{11}+iS_{21})u_+(r) \quad (30)$$

$$u_{12}(r)+iu_{22}(r)\sim i[-u_-(r)+(S_{22}-iS_{12})u_+(r)] \quad (31)$$

shows that the scattering coefficient S_l of the outgoing spherical wave can be expressed in terms of the two-dimensional S-matrix as

$$\begin{aligned} S_l &= S_{11}+iS_{21} \\ &= S_{22}-iS_{12} \end{aligned} \quad (32)$$

which produces a scattering amplitude given by equation (16).

2.2. *Potential Calculation*

To carry out the scattering calculations, we need to specify the potential $V(r)$ (eq. [21]). In both neighboring and central atom scattering problems, $V(r)$ can be represented by the electrostatic potential $V_0(\boldsymbol{r})$, consisting of nuclear point-charge and electron charge density, plus the self-energy potential U, which is the effective scattering potential due to exchange and correlation effects of electrons in the atom.

The electrostatic potential of the neutral atom is

$$V_0(\boldsymbol{r})=-\frac{Z}{r}+\int\frac{\rho_e(\boldsymbol{r}')}{|\boldsymbol{r}-\boldsymbol{r}'|}\,d\boldsymbol{r}'\ , \quad (33)$$

where Z is the nuclear charge of the atom and $\rho_e(\boldsymbol{r})$ is the electron charge density function. $\rho_e(\boldsymbol{r})$ was obtained from density functional theory using the local density approximation by solving the self-consistent relativistic Kohn-Sham equation (Kohn & Sham 1965). The electron charge density function is normalized to be $\int\rho_e(\boldsymbol{r})d\boldsymbol{r}=Z$. In the atom with a core hole, there are two contributions to the electrostatic potential: one from the ionized atom and the other from the screening potential of the surrounding medium. The contribution to the electrostatic potential from the ionized atom is

$$V_0^1(\boldsymbol{r})=-\frac{Z}{r}+\int\frac{\tilde{\rho}_e(\boldsymbol{r}')}{|\boldsymbol{r}-\boldsymbol{r}'|}\,d\boldsymbol{r}'\ , \quad (34)$$

where $\tilde{\rho}_e(\boldsymbol{r})$ is now normalized to be $\int\tilde{\rho}_e(\boldsymbol{r})d\boldsymbol{r}=Z-1$ and is obtained by solving the Kohn-Sham equation with one $1s$ electron missing. The screening potential is approximated by

$$V_0^2(\boldsymbol{r})=\frac{1-e^{-r/\lambda_a}}{r}\ , \quad (35)$$

where $\lambda_a\approx 2r_a$ with r_a the effective radius of the atom. Since the screening potential goes to $1/r$ for $r\gg\lambda_a$, an extra screening electron is effectively added to the ionized atom to cancel out the core hole charge. Thus, the resulting electrostatic potential of the ion is

$$V_0(\boldsymbol{r})=-\frac{(Z-1)+e^{-r/\lambda_a}}{r}+\int\frac{\tilde{\rho}_e(\boldsymbol{r}')}{|\boldsymbol{r}-\boldsymbol{r}'|}\,d\boldsymbol{r}'\ . \quad (36)$$

For the self-energy potential U, we have adopted the formulation of Lee & Beni (1977). Since U is relatively small compared to the Fermi energy $\frac{1}{2}k_{\mathrm{F}}^2$, we assume

$$\tfrac{1}{2}p^2(r)=\tfrac{1}{2}k^2+\tfrac{1}{2}k_{\mathrm{F}}^2\ , \quad (37)$$

where k is the momentum of the electron outside the atom and k_F is the Fermi momentum. Then, the complex self-energy potential $U[\boldsymbol{p}, w=\frac{1}{2}p^2(r)]$ can be computed in the plasmon pole approximation, which replaces the elementary excitation of an electron gas by a single pole. The real part of the self-energy potential is given by

$$\mathrm{Re}\ U(\boldsymbol{p},w)=-\int\frac{d\boldsymbol{q}}{(2\pi)^3}\frac{4\pi}{q^2}\left\{\frac{f(\boldsymbol{p}+\boldsymbol{q})}{\epsilon[q,\frac{1}{2}(\boldsymbol{p}+\boldsymbol{q})^2-w]}-\frac{w_p^2}{2w_1(q)[w_1(q)-w+\frac{1}{2}(\boldsymbol{p}+\boldsymbol{q})^2]}\right\}, \quad (38)$$

where

$$\epsilon(q, \tilde{w})^{-1} = 1 + \frac{w_p^2}{\tilde{w}^2 - w_1^2(q)}, \tag{39}$$

$$w_1^2(q) = w_p^2 + \epsilon_F^2\left[\frac{4}{3}\left(\frac{q}{\epsilon_F}\right)^2 + \left(\frac{q}{\epsilon_F}\right)^4\right]. \tag{40}$$

$f(\boldsymbol{q})$ is the Fermi distribution function and w_p is the plasma frequency. The imaginary part is given by

$$\begin{aligned}\mathrm{Im}\ U(\boldsymbol{p}, w) = \frac{\pi w_p^2}{2}\int \frac{d\boldsymbol{q}}{(2\pi)^3}\frac{4\pi}{q^2}\frac{1}{w_1(q)} \\ \times\left\{f(\boldsymbol{p}+\boldsymbol{q})\delta\left[\frac{1}{2}(\boldsymbol{p}+\boldsymbol{q})^2 - w_1(q) - w\right]\right. \\ \left. + [1 - f(\boldsymbol{p}+\boldsymbol{q})]\delta\left[\frac{1}{2}(\boldsymbol{p}+\boldsymbol{q})^2 + w_1(q) - w\right]\right\}.\end{aligned} \tag{41}$$

3. AEA TOOL AND DATA BASE

We have built the AEA tool for the astrophysics community to be able to construct an EXAFS numerical model of a given compound by a simple procedure without the need to consider the underlying mathematical and numerical detail. The AEA tool is able to calculate $\chi(k)$, the modification to the X-ray absorption coefficient due to EXAFS, from the user-provided list of atomic numbers of neighboring atoms and their distances to the central X-ray–absorbing atom. A UNIX tar file of the AEA tool can be obtained by the UNIX anonymous ftp; the ftp site of the most recent version can be identified by sending an e-mail to jwoo@cfa.harvard.edu.

The AEA tool provides a complete set of EXAFS parameters, $2\delta_1$, ϕ_b, and F (as defined in eq. [20]) for the elements with atomic numbers up to 92 as a function of k between 2 and 8 atomic units (3.78–15.12 Å^{-1}) in steps of 0.1 atomic units. In Figure 1, we have compared our numerical results with the numerical model of Teo & Lee (1979). Although our computer software has been developed completely independent of Teo & Lee's (with similar mathematical formalism according to Lee & Beni 1977), these two results are quite similar. This similarity establishes a useful calibration for our AEA tool.

The AEA tool provides a program called "calExafs" which calculates the modification to the X-ray absorption coefficient, $\chi(k)$ (eq. [20]) using the provided EXAFS parameter data set ($2\delta_1$, ϕ_b, and F). The "calExafs" program has an option to correct the normalization factor of $\chi(k)$ for the inelastic scattering losses (see § 4.2 for details); for our two examples (in §§ 3.1 and 3.2), we have assumed 74% to be our normalization as suggested by Lee & Beni (1977). The program requires an input file that contains the structural information of the desired compound. The structure input file is required to have the atomic number of the central X-ray–absorbing atom and two columns of numbers; the first column is the atomic number of the backscattering atom, and the second column is the spacing (in units of Å) between the central X-ray–absorbing atom and the backscattering atom. The structural information of most compounds can be easily obtained from standard literature (see, e.g., Wilson 1955). In the rest of this section, we show the results from the AEA tool for two examples: SiO_2 and $MgSiO_3$.

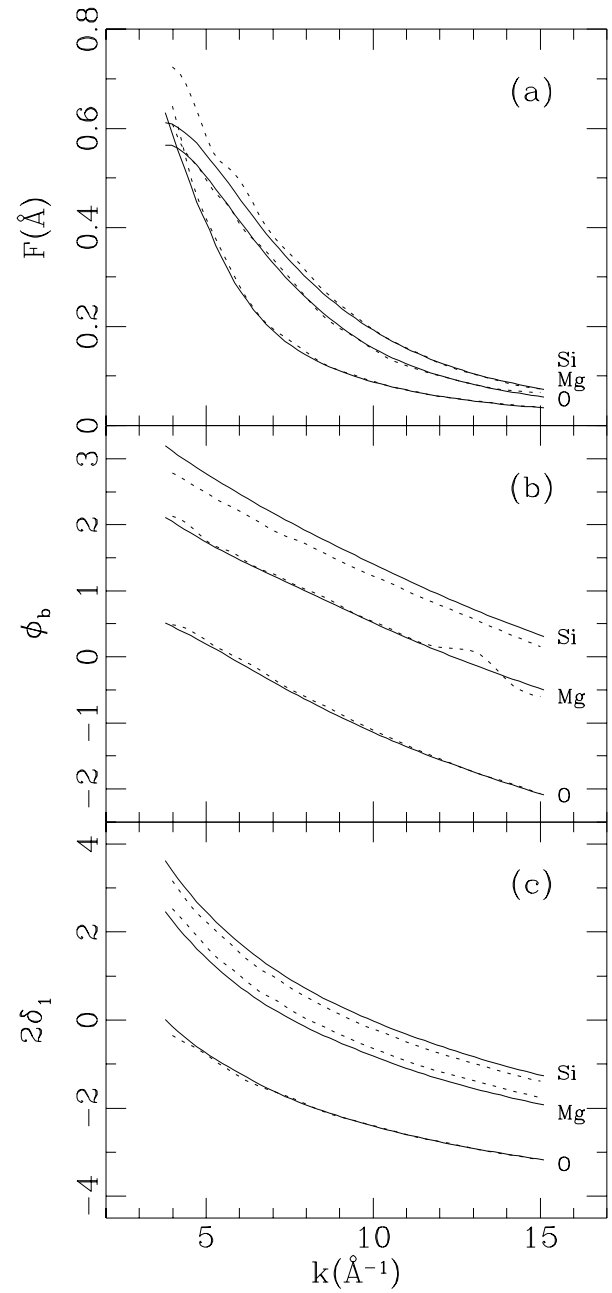

FIG. 1.—Comparison of the numerical results from the AEA tool (*solid lines*) with those from the Teo & Lee (1979) model (*dotted lines*) for O, Mg, and Si: (*a*) backscattering amplitude function; (*b*) backscattering phase function; (*c*) X-ray absorber phase function.

3.1. SiO_2

We have selected α-quartz ($3SiO_2$) as our first example of the numerical EXAFS model. α-quartz has a hexagonal unit cell that is made of three SiO_2 molecules. It also has connected tetrahedrals that are made of one O and four Si atoms. In the tetrahedral structure, each Si atom is bonded with two adjacent O atoms while each O atom is bonded with four Si adjacent atoms. For simplicity, we assume that any given O atom in the α-quartz is positioned at the center of two tetrahedrals where the inner tetrahedral is made of four Si atoms and the outer tetrahedral is made of four O atoms. We also assume that the average separation between the central O atom and Si atoms is 1.6 Å and that the

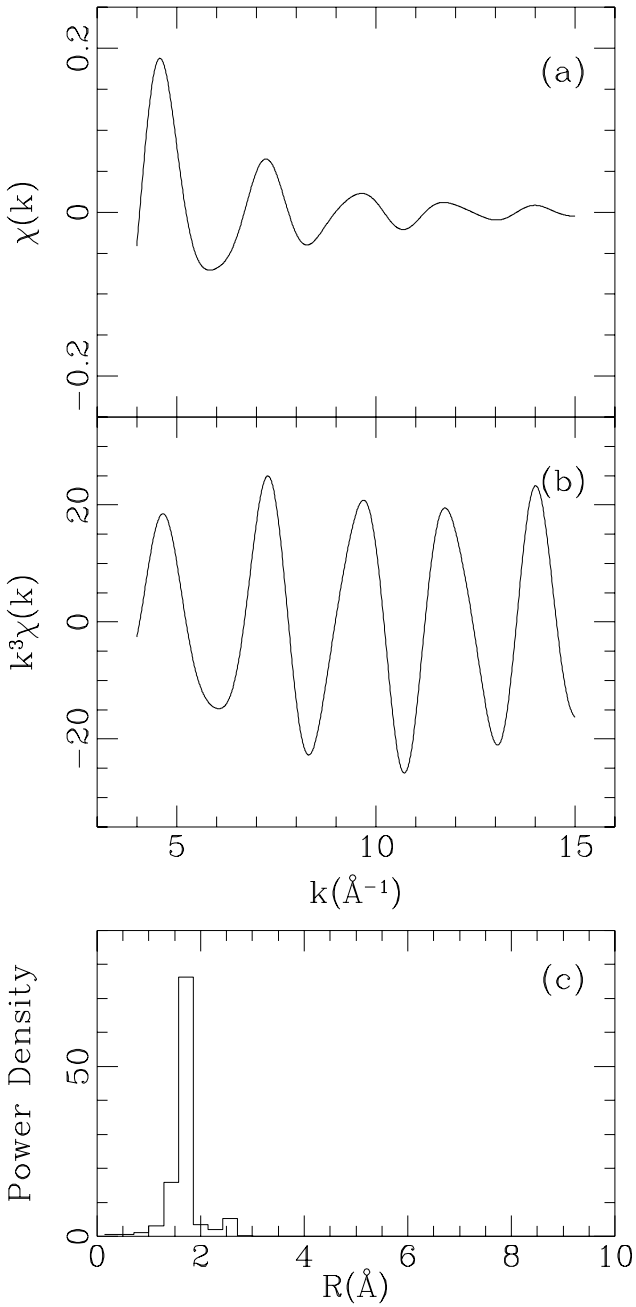

FIG. 2.—Predicted O K-edge EXAFS of SiO_2 from the AEA tool: (*a*) $\chi(k)$; (*b*) $k^3\chi(k)$; (*c*) power density spectrum of (*b*).

average separation between the central O atom and outer O atoms is 2.6 Å. Figure 2 shows the result of EXAFS calculation of O K edge using the AEA tool. Our predicted $\chi(k)$ and $k^3\chi(k)$ spectra are shown in Figures 2*a* and 2*b*. In Figure 2*c*, we have plotted the power density spectrum of $k^3\chi(k)$ of Figure 2*b*. A quick demonstration of our data analysis technique shows that we can easily recover 1.6 and 2.6 Å peaks from the power density spectrum.

3.2. $MgSiO_3$

Our second model is Enstatite ($2MgSiO_3$), which has an orthorhombic crystal structure (see, e.g., Wilson 1955). Using the positional information of two $MgSiO_3$ molecules in the unit cell (Table 1), we have constructed a complete list of atomic numbers and distances from the two Mg atoms in the central unit cell to 538 neighboring atoms in the unit cell plus 26 duplicated cells that completely surround the central unit cell. This list should cover any significant single scattering path to neighboring atoms. The result of calculated EXAFS $\chi(k)$ spectrum above Mg K edge by the AEA tool using the above list is shown in Figure 3. As before, we show the predicted $\chi(k)$ and $k^3\chi(k)$ spectra in Figures 3*a* and 3*b* and the power density spectrum of $k^3\chi(k)$ in Figure 3*c*. Unlike the SiO_2 case, we see high-order features in the $\chi(k)$ spectra and high-order (or large R) peaks in the power density spectrum because of 26 duplicated cells that surround the central unit cell. From the power density spectrum of Enstatite, similar to the α-quartz case, we can also recover the positions of O atoms at ≈2.1 Å, Mg and Si atoms at ≈3.2 Å, O atom at ≈3.5 Å, and O and Si atoms at ≈5.1 Å (as listed in Table 1).

TABLE 1

COORDINATE POSITIONS OF INDIVIDUAL ELEMENTS AND DISTANCES FROM THE TWO Mg ATOMS TO EACH OF THE ATOMS IN $2MgSiO_2$ (WILSON 1955)

Atom	x	y	z	d^a (Å)	d^b (Å)
Mg^1	0.125	0.333	0.375	0.000	3.251
Mg^2	0.125	−0.036	0.375	3.251	0.000
Si	0.028	−0.336	0.267	3.229	6.179
	0.222	−0.172	0.028	2.798	5.117
O	0.061	0.147	0.219	2.149	2.169
	0.061	0.503	0.200	4.974	2.106
	0.058	−0.267	0.000	3.074	5.766
	0.189	0.347	0.028	4.001	2.155
	0.197	0.006	0.050	2.174	3.590
	0.194	−0.236	0.292	2.207	5.186
Unit axis (Å).....	18.22	8.81	5.21	...	...

[a] Distances from Mg^1.
[b] Distances from Mg^2.

4. DISCUSSION

4.1. *Gaussian Damping Term*

Static structural disorder and thermal vibration are two components that modify EXAFS and can be represented by a Gaussian function with the Debye-Waller factor σ. With the Gaussian term, the EXAFS form becomes

$$\chi(k) = \sum_j F_j(k) \frac{\sin\,[2kr_j + \eta_j(k)]}{kr_j^2}\, e^{-2k^2\sigma_j^2} . \qquad (42)$$

It is nontrivial to model the Debye-Waller factor because it depends on the particular process by which a given material is produced and its environment.

For astrophysical grains, we can ignore thermal vibrations due to the cold temperature of interstellar space (e.g., $T \sim 10$–100 K). The measured σ factor of the EXAFS signal from the astrophysical grains, therefore, contains information on the static structural disorder of the grains. By measuring EXAFS from crystalline, polycrystalline, and amorphous laboratory samples—prepared in a low-temperature environment to have the same composition as the interstellar grains, we should be able to model the Debye-Waller factors for the different structural types of the interstellar grains using equation (42). If we compare these tabulated Debye-Waller factors of the different structural types with the observed factor of the grains, we should be able to learn about the internal structure of the interstellar grains.

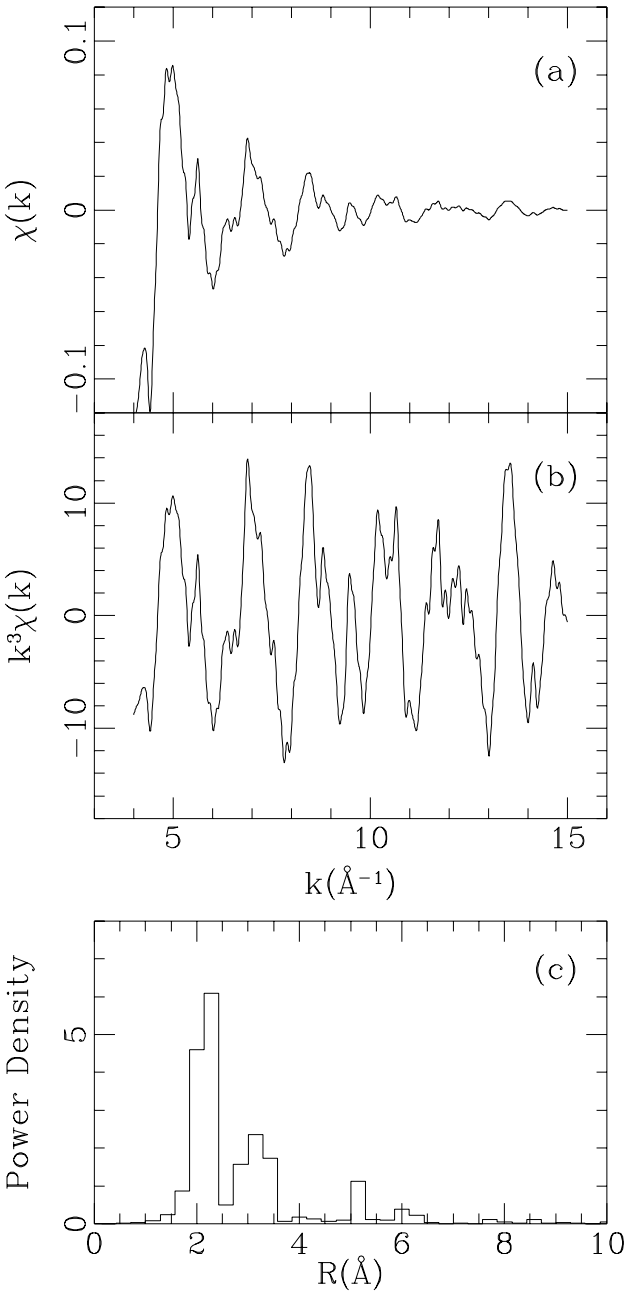

FIG. 3.—Predicted Mg K-edge EXAFS of $MgSiO_3$ from the AEA tool: (*a*) $\chi(k)$; (*b*) $k^3\chi(k)$; (*c*) power density spectrum of (*b*).

4.2. *Inelastic Scattering Losses*

There are two inelastic scattering contributions in our scattering calculation. The first one is represented by the absorption factor (eq. [24]) that comes from the central-atom scattering calculation. The second one is due to the relaxation of the core hole, which is dominated by the Auger processes. Although we obtain the absorption factor (eq. [24]) from our central-atom scattering calculation, it is extremely difficult to calculate the inelastic scattering amplitude of the Auger process (Cho & Oh 1989). Since both inelastic contributions involve the same final state, they must be added coherently. Therefore, the absorption factor (eq. [24]) alone cannot make a meaningful contribution. To circumvent the difficulty, the overall magnitude of the inelastic scattering is typically fitted to experimental data. Estimates by Lee & Beni (1977) indicate that at very high energies where $\mathrm{Im}(\delta_l)$ is small, only about 74% of the photoelectrons have been excited elastically. In the present version of our database, we have chosen to follow the Lee & Beni (1977) estimate of 74% for our normalization. In later versions, we hope to address the issue of core hole relaxation more rigorously.

5. CONCLUSION

The analysis and corresponding database that is described in this paper is the first step toward applying the well-known EXAFS theory to astrophysical objects such as interstellar dust grains. Readers familiar with the condensed matter literature on EXAFS theory may recognize that much remains to be done before the project can be considered complete. For example, the plane wave approximation that was used in § 2 should be replaced by a more accurate spherical wave approximation. The multiple scattering contributions that become important at low energies should be included in the analysis/database, and a more detailed treatment of the inelastic effects should be provided. Despite these shortcomings, we feel that the present work represents a pivotal step in providing the astrophysical community with the necessary tools to study the next generation of observed interstellar X-ray spectra.

We thank Alex Dalgarno and Kate Kirby for their careful review of the manuscript and useful comments. This research was supported in part by grant NAS 8-39073 from the National Aeronautics and Space Administration. The work of R. C. F. was supported by the US Department of Energy.

REFERENCES

Cho, K., & Oh, S. J. 1989, Phys. Rev. B, 39, 9576
Cho, K., & Woo, J. W. 1997, in preparation
Evans, A. 1986, MNRAS, 223, 219
Joachain, C. J. 1975, Quantum Collision Theory (Amsterdam: North-Holland)
Kohn, W., & Sham, L. J. 1965, Phys. Rev., 140, A1133
Kossel, W. 1920, Z. Phys., 1, 119
Kronig, R. de L. 1931, Z. Phys., 70, 317
Lee, P. A., & Beni, G. 1977, Phys. Rev. B, 15, 2862
Lee, P. A., & Pendry, J. B. 1975, Phys. Rev. B, 11, 2795
Martin, P. G. 1970, MNRAS, 149, 221
Owens, A., Denby, M., Wells, A., Keay, A., Graessle, D. E., & Blake, R. L. 1997, ApJ, 476, 924
Sayers, D. E., Stern, E. A., & Lytle, F. 1971, Phys. Rev. Lett., 27, 1204
Teo, B. K., & Lee, P. A. 1979, J. Am. Chem. Soc., 101, 2815
Wilson, A. J. C., ed. 1955, Structure Reports for 1942–1944, Vol. 9 (Utrecht: Int. Union Crystallogr.), 254
Woo, J. W. 1995, ApJ, 447, L129